Journal of Rock Mechanics and Geotechnical Engineering 14 (2022) 757–769

Contents lists available at ScienceDirect

Journal of Rock Mechanics and Geotechnical Engineering

journal homepage: www.jrmge.cn

Full Length Article

Fracture of two three-dimensional parallel internal cracks in brittle solid under ultrasonic fracturing

Haijun Wang [a], Hanzhang Li [a], Lei Tang [a,*], Xuhua Ren [b], Qingxiang Meng [b], Chun Zhu [b,**]

[a] State Key Laboratory of Hydrology-Water Resources and Hydraulic Engineering, Nanjing Hydraulic Research Institute, Nanjing, 210029, China
[b] School of Earth Sciences and Engineering, Hohai University, Nanjing, 210098, China

ARTICLE INFO

Article history:
Received 15 July 2021
Received in revised form
19 September 2021
Accepted 21 November 2021
Available online 6 December 2021

Keywords:
Three-dimensional internal laser-engraved crack (3D-ILC)
Interaction of cracks
Ultrasonic fatigue
Penny-shaped crack
Fracture mechanics
High-cycle fatigue

ABSTRACT

Similar to hydraulic fracturing (HF), the coalescence and fracture of cracks are induced within a rock under the action of an ultrasonic field, known as ultrasonic fracturing (UF). Investigating UF is important in both hard rock drilling and oil and gas recovery. A three-dimensional internal laser-engraved crack (3D-ILC) method was introduced to prefabricate two parallel internal cracks within the samples without any damage to the surface. The samples were subjected to UF. The mechanism of UF was elucidated by analyzing the characteristics of fracture surfaces. The crack propagation path under different ultrasonic parameters was obtained by numerical simulation based on the Paris fatigue model and compared to the experimental results of UF. The results show that the 3D-ILC method is a powerful tool for UF research. Under the action of an ultrasonic field, the fracture surface shows the characteristics of beach marks and contains powder locally, indicating that the UF mechanism includes high-cycle fatigue fracture, shear and friction, and temperature load. The two internal cracks become close under UF. The numerical result obtained by the Paris fatigue model also shows the attraction of the two cracks, consistent with the test results. The 3D-ILC method provides a new tool for the experimental study of UF. Compared to the conventional numerical methods based on the analysis of stress–strain and plastic zone, numerical simulation can be a good alternative method to obtain the crack path under UF.

1. Introduction

The disturbance from nature or rock engineering applications, e.g. cyclic wetting-drying (Li et al., 2021a, b), excavation with different loading rates (Gao et al., 2021a), preloading which can induce creep of rock mass (Shi et al., 2019), and reinforcement work on the rock surfaces (Li et al., 2021a,b,c,d,e), can influence the mechanical properties of the rock mass to a great extent. The ultrasonic loading used in gas and oil industry is characterized by the high frequency compared with other loading forms. Under the action of an ultrasonic field, microcracks in brittle solid will grow, causing fracture, known as ultrasonic fracturing (UF), similar to hydraulic fracturing (HF). Rock is a typical brittle material with many microcracks or crack-like defects. Under the action of ultrasound, crack propagation deteriorates the rock mass, thus significantly reducing the difficulty of drilling in deep hard rock. During this process under ultrasonic action, network channels of cracks are formed, thus increasing the permeability of the rock, making UF as an important method to improve oil and gas recovery (Gao et al., 2021b). Therefore, studies on UF are important in both oil and gas exploration and hard rock drilling.

Towards investigating the interaction of multiple cracks, Lin et al. (2020a, b, 2021) carried out a series of experiment and numerical simulation studies. Types of penetrating crack coalescence under uniaxial compression in rock-like material with two dissimilar layers or double circular openings were investigated in detail. Nevertheless, a mass of cracks is located in the interior part of the rock known as internal cracks, and the cracks should propagate in three dimensions. The crack networks formed under ultrasound action are also located inside the rock. Therefore, the interaction of multiple internal cracks in UF is unavoidable and must be investigated thoroughly. However, physical experiments and theoretical analysis of UF pose many challenges.

* Corresponding author.
** Corresponding author.
E-mail addresses: ltang@nhri.cn (L. Tang), zhuchuncumtb@163.com (C. Zhu).
Peer review under responsibility of Institute of Rock and Soil Mechanics, Chinese Academy of Sciences.

https://doi.org/10.1016/j.jrmge.2021.11.002

The growth process of internal cracks is invisible, because they are located in the internal part of the rock mass like in a "black box." At present, crack growth under UF has not been described. Zhao and Yuan (2018) and Tang et al. (2016) used T2 spectrum and porosity to characterize the effect of UF. Xiao et al. (2013) observed the distribution of the number of macrocracks after ultrasonic treatment by CT scanning. So far, the macroscopic parameters such as uniaxial compressive strength and permeability did not clarify the propagation of three-dimensional (3D) internal cracks inside rocks under the UF effects. Therefore, transparent brittle materials have been extensively used for simulating rocks to study the internal crack propagation and the interaction between multiple internal cracks. Three most commonly applied methods are (1) cut-and-paste method (Adams and Sines, 1978); (2) embedded casting method (Dyskin et al., 1994; Fu et al., 2016), as shown in Fig. 1; and (3) 3D printing method (Ju et al., 2014; Zhou et al., 2019), as shown in Fig. 2. However, these methods suffer from many problems. In Method 1, the integrity of the sample is destroyed. In Method 2, which is mostly used at present, the brittleness of the material is very low, because the material shows plasticity even at very low temperatures. In addition, aluminum flakes or thin mica sheets are used to simulate internal cracks, which are not true cracks. In Method 3, the brittleness of the material is very low as well, because the material is still of resinous type. The other problem is that the simulated internal crack is actually a flat cylinder filled with a liquid polymer with a height of ~2 mm, because of the minimum scanning thickness of UV. In order to address this problem, Wang et al. (2019) introduced the 3D internal laser-engraved crack (3D-ILC) method for manufacturing closed internal cracks within transparent brittle solids. The practicability of the 3D-ILC method has been experimentally proved based on the related studies previously reported (Wang et al., 2021; Li et al., 2021a, b, c, d, e).

Numerical simulation has been extensively used to study the internal crack propagation inside rocks (Wang et al., 2020a, b; Han et al., 2021; Li et al., 2021a, b, c, d, e). Zhou et al. (2016) developed HF modeling using PFC2D software, and a series of HF simulation studies was carried out, indicating that the propagation of HF is controlled by both the in situ stress state and strength anisotropy of the reservoir rock. Some researchers (Nezhad et al., 2018) proposed a modeling framework based on a variational method, and the crack propagation in shale under Brazilian disk test was reproduced. Yang et al. (2020) used PFC software to simulate the crack propagation during synchronous fracturing and investigated the rock failure mode and crack propagation mechanism under different perforation angles and arrangements. Numerical simulation on the growth of internal cracks in UF is rare at present. Chen et al. (2017) used numerical simulations of ultrasound transmission

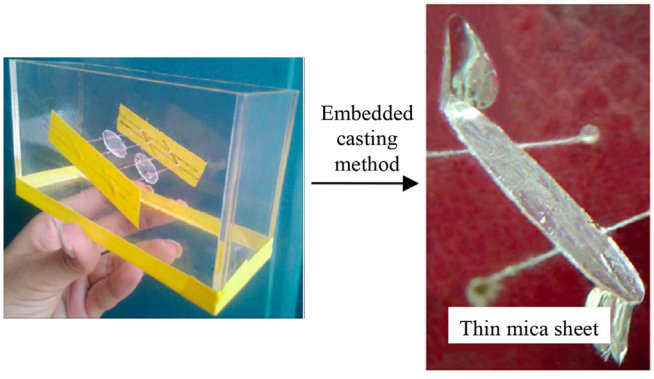

Fig. 1. Embedded casting method.

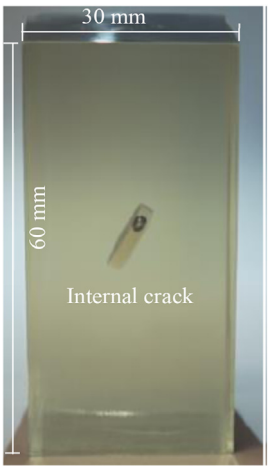

Fig. 2. 3D printing method.

experiments on shale using the high-order staggered-grid finite difference method in MATLAB. Tang et al. (2020) used the discrete element method (DEM) to elucidate the fragmentation mechanism of rocks under ultrasonic vibration. Huang et al. (2018) used a K-body (dashpot contact with spring) to construct a constitutive model. However, these models are macroscopic rheological models and do not involve crack propagation. In summary, there are few simulation reports on the fracture path of cracks under UF effects.

Therefore, in this study, we developed an innovative 3D-ILC technology for producing internal cracks inside glass without damaging the surface. Then, the behavior of two penny-shaped internal cracks was investigated by both physical experiments and numerical simulations, and the growth path, attraction and the surface characteristics of the two internal cracks under UF effects were obtained and analyzed, elucidating the working mechanism of UF on rock breaking. Finally, the attraction of two parallel internal cracks under UF was determined by 3D numerical simulation, and the mechanism and feasibility of rock breaking by ultrasonic wave were further elucidated. These results will provide new experimental and numerical simulation methods for the future studies of UF in brittle solids.

2. Experimental setup

2.1. 3D-ILC method for producing internal cracks

This study, unlike the previous method of prefabricating cracks in transparent materials, proposed a 3D-ILC method (Wang et al., 2019), and the internal cracks were directly generated in brittle solids without any damage to the surface of the sample, as shown in Fig. 3. The basic principle of the 3D-ILC method is as follows. The laser is focused on the interior of the medium, and the energy at the laser focus points exceeds the dielectric damage threshold. As a result, plasma blasting points are formed, and a large number of connected blasting points caused a "dielectric breakdown area" in the medium. The second basic principle is that the high-frequency laser thermal shockwaves form fatigue "crack propagation rings," and the crack tips are smooth and neat. The smooth and neat "crack rings" are the major difference between the introduced 3D laser thermal fatigue method and the previous methods.

The 3D-ILC method was performed as follows. The internal cracks were designed, and their numerical simulation was carried out, in which a computer-controlled femtosecond pulse laser was shot into the glass by focusing the lens at the locations of

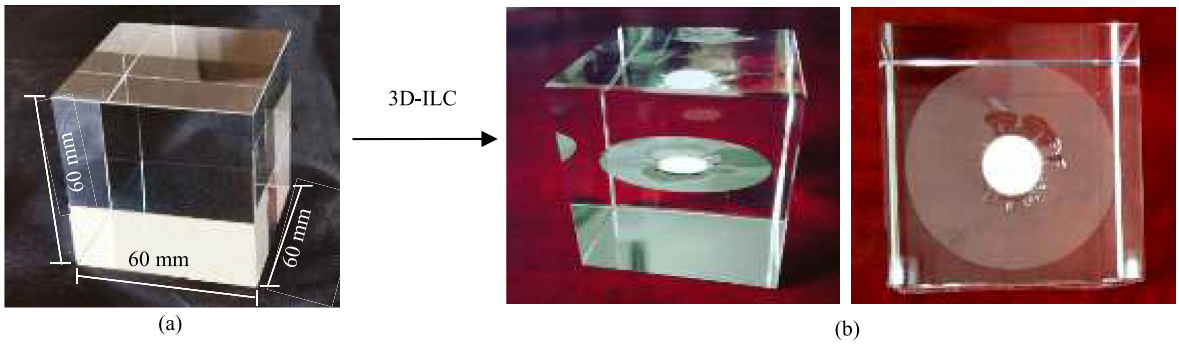

Fig. 3. 3D-ILC method for producing internal cracks: (a) Intact sample, and (b) Sample with internal crack.

prefabricated cracks in the material. A large number of pulses were focused at the blasting points for forming a dielectric breakdown area, which is visually white in color. Then, fatigue crack propagation occurred in the outward direction at the fracture edges. The crack tips were observed to be smooth and neat, forming a "crack propagation ring," which then connected with the "dielectric breakdown area" to form a macroscopic 3D internal crack. Moreover, the remainder of the transparent material did not show any change. Because the cracks in this study were generated by the propagation of cracks under loading action, the authenticity of the internal cracks was achieved.

2.2. Material and parameters of sample

Glass was selected as the experiment material attributing the following advantages: (1) It is the material with ideal homogeneity and isotropy and strictly follows Hooke's law before crack growth. Therefore, Griffith and Taylor (1921) first time used glass as an experimental material in brittle fracture, and it has been used until now for a span of one century. (2) Regarding the brittleness, the tension to compression ratios of the glass can potentially reach between 1/13 and 1/33, similar to that of an actual rock (1/12 to 1/35). Therefore, glass can be used to effectively simulate the brittleness of rocks (Germanovich et al., 1994). (3) The characteristics of glass fracture are very obvious, and thus can be used to analyze the physical mechanisms of the fracture. In this study, the K9 glass, a borosilicate optical crown glass, was used as the sample material for its excellent transparency compared with that of soda-lime glass. It is undeniable that K9 glass has limitations, such as excessive brittleness, homogeneity and isotropy on simulating real rocks in laboratory setting. Nevertheless, compared with other rock-like materials, it still shows better brittleness and transparency. The mechanistic analysis of UF was carried out based on fractography. The sample is a cube with a dimension of 60 mm × 60 mm × 60 mm; the internal crack is circular with a diameter of 10 mm. As to the relative position relation, l and d are defined as the horizontal distance and perpendicular distance of the centers of the two internal cracks, respectively. The design drawing and actual sample are shown in Fig. 4.

2.3. Ultrasonic loading system

The ultrasonic loading system comprises an ultrasonic generator, a transducer, and a horn (amplitude transformer), as shown in Fig. 5. Ultrasonic generator is also known as an ultrasonic power source. It converts 220 V, 50 Hz alternating electric energy into ultrasonic frequency electric energy (frequency ≥20 kHz) using analog or digital circuits and transmits the energy to a transducer. The transducer converts ultrasonic frequency electrical energy into the mechanical energy of ultrasonic vibration. At this time, the ultrasonic amplitude generated by the radiation surface of transducer is small, making it difficult to satisfy the application requirements. The horn can amplify the displacement and movement speed of mechanical vibration particles and intensify the ultrasonic energy to satisfy the requirements of high-intensity ultrasound applications, after which it transmits it to various tool heads or specimens to achieve the ultrasonic treatment of the specimen. In this test, the ultrasonic frequency was set as 28 kHz. The incident direction of the ultrasonic wave is perpendicular to the biparallel internal crack surface. The fracture surface was observed using an optical microscope (Zeiss Axio Scope A1), as shown in Fig. 5d.

3. Experimental results

3.1. Growth of two cracks and morphological characteristics

3.1.1. Growth and attraction between two cracks

Under the action of ultrasound, first, the upper crack begins to crack, followed by the lower crack, because the upper crack is closer to the ultrasonic oscillator. After the two cracks started to crack, they initially spread outward in a separate plane, exhibiting a circle growth shape, because the bulk region between the two cracks is large enough to allow the line of maximum tension to be aligned

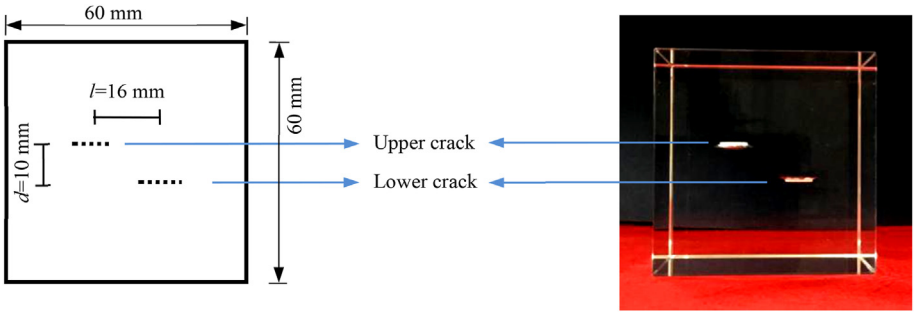

Fig. 4. Samples with internal cracks.

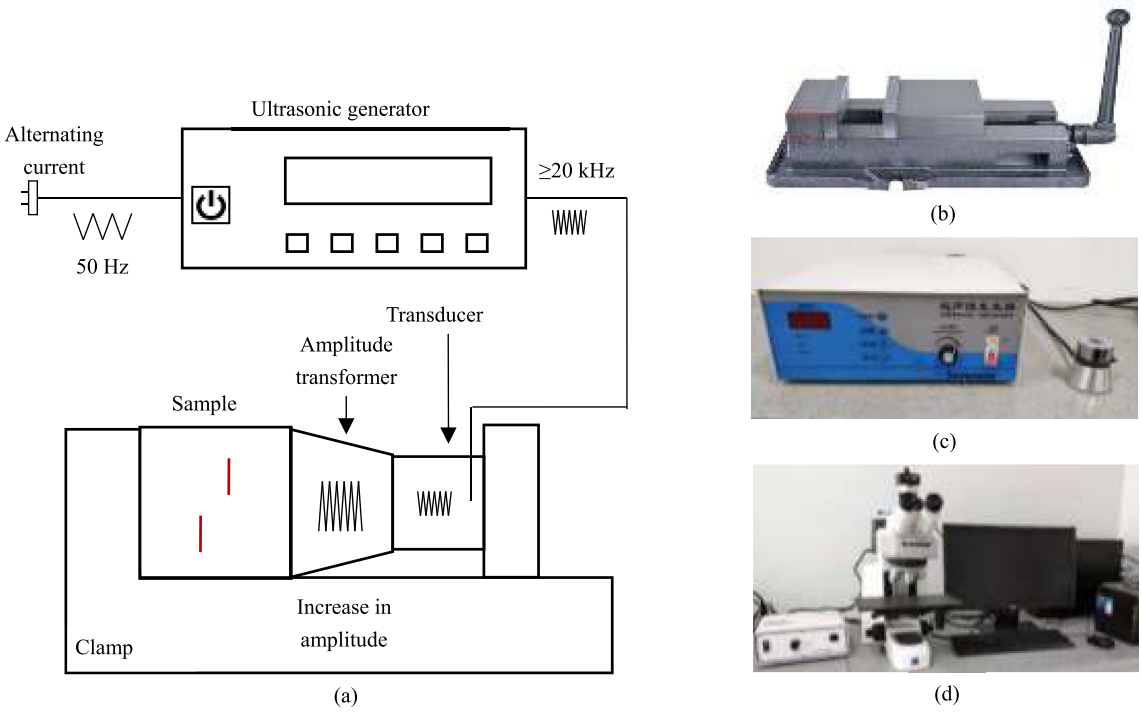

Fig. 5. Ultrasonic loading system: (a) Sketch of ultrasonic testing system, (b) Picture of the clamp, (c) Picture of ultrasonic generator and transducer, and (d) Picture of optical microscope.

with the boundary loading as Fender et al. (2010) proposed. At this stage, the interaction of multiple cracks can be neglected, and pure mode I fracture is the main feature. Then, when the two cracks grow close to each other, the double cracks appear and "attract" each other. The growth paths of the two cracks begin to approach each other, forming a "hook shape", leading to contact. At this stage, the stress field between the two crack tips is distorted, and shear stress rotates the direction of crack growth to the plane vertical to the maximum tension. The crack growth mode transformed from pure mode I to mixed mode I-II fracture, as shown in Fig. 6. In fact, ultrasound excitation provides considerable shear stress, and its effects are discussed in Section 3.2. The mutual attraction between double cracks under the action of ultrasound is consistent with that of double parallel cracks under uniaxial tension (Dalbe et al., 2015; Schwaab et al., 2018; Yu et al., 2019), as shown in Fig. 7.

Because the attraction of two cracks is the superposition of modes I and II loading, the stress intensity factors (SIFs) at the crack tips can be expressed as follows:

$$\left.\begin{aligned} K'_{\mathrm{I}}(\theta) &= K_{\mathrm{I}} f^{\mathrm{I}}_{\theta\theta} + K_{\mathrm{II}} f^{\mathrm{II}}_{\theta\theta} \\ K'_{\mathrm{II}}(\theta) &= K_{\mathrm{I}} f^{\mathrm{I}}_{r\theta} + K_{\mathrm{II}} f^{\mathrm{II}}_{r\theta} \\ K'_{\mathrm{III}}(\theta) &= 0 \end{aligned}\right\} \tag{1}$$

where K_{I} and K_{II} are the modes I and II SIFs, respectively; $K'_{\mathrm{I}}(\theta)$, $K'_{\mathrm{II}}(\theta)$ and $K'_{\mathrm{III}}(\theta)$ are the transformed SIFs; and f_{ij} is an angle function denoted as follows:

$$\left.\begin{aligned} f^{\mathrm{I}}_{\theta\theta} &= \cos^3(\theta/2) \\ f^{\mathrm{I}}_{r\theta} &= \sin(\theta/2)\cos^2(\theta/2) \\ f^{\mathrm{II}}_{\theta\theta} &= -3\sin(\theta/2)\cos^2(\theta/2) \\ f^{\mathrm{II}}_{r\theta} &= \cos(\theta/2)\left[1-3\sin^2(\theta/2)\right] \end{aligned}\right\} \tag{2}$$

Therefore, the angular variation of mechanical energy release rate can be expressed as follows:

$$G(\theta) = K'^2_{\mathrm{I}}(\theta)\left(1-\nu^2\right)\Big/E + K'^2_{\mathrm{II}}(\theta)\left(1-\nu^2\right)\Big/E \tag{3}$$

where $G(\theta)$ is the mechanical energy release rate at angle θ, ν is the Poisson's ratio, and E is the elasticity modulus. Fig. 8b shows the normalized plots of mechanical energy release rate varying with deflection angle. The imposed shear arises from the variation of stress field. Ultrasonic excitation deflects the crack away from the initial plane of the internal cracks, and the deflection always lies toward the direction of minimum shear stress, i.e. the shear stress may correct the crack growth direction, restoring deviant cracks to a stable path that is vertical to the maximum principal tensile stress at the crack tips.

3.1.2. *Speed of crack growth and fracture morphological characteristics*

As shown in Fig. 9, under UF, the speed and surface of double crack growth follow the following rules:

(1) The growth speed of the upper crack is greater than that of the lower crack, because it is closer to the ultrasonic oscillator.
(2) As the propagation speed is different at the end of the test, the growth area of the upper crack is significantly larger than that of the lower crack.
(3) In the mutual attraction area, the upper crack propagates toward the lower crack. The top view shown in Fig. 9 indicates a "heart-shaped" pattern of the growth zone of the upper crack.
(4) In the mutual attraction zone, the upper crack propagation speed is less than that in other locations. The "recessed" arcs in the attraction zone show that the density of cracks is shorter than that in other locations. This phenomenon further forms a "heart-shaped" expanded pattern.

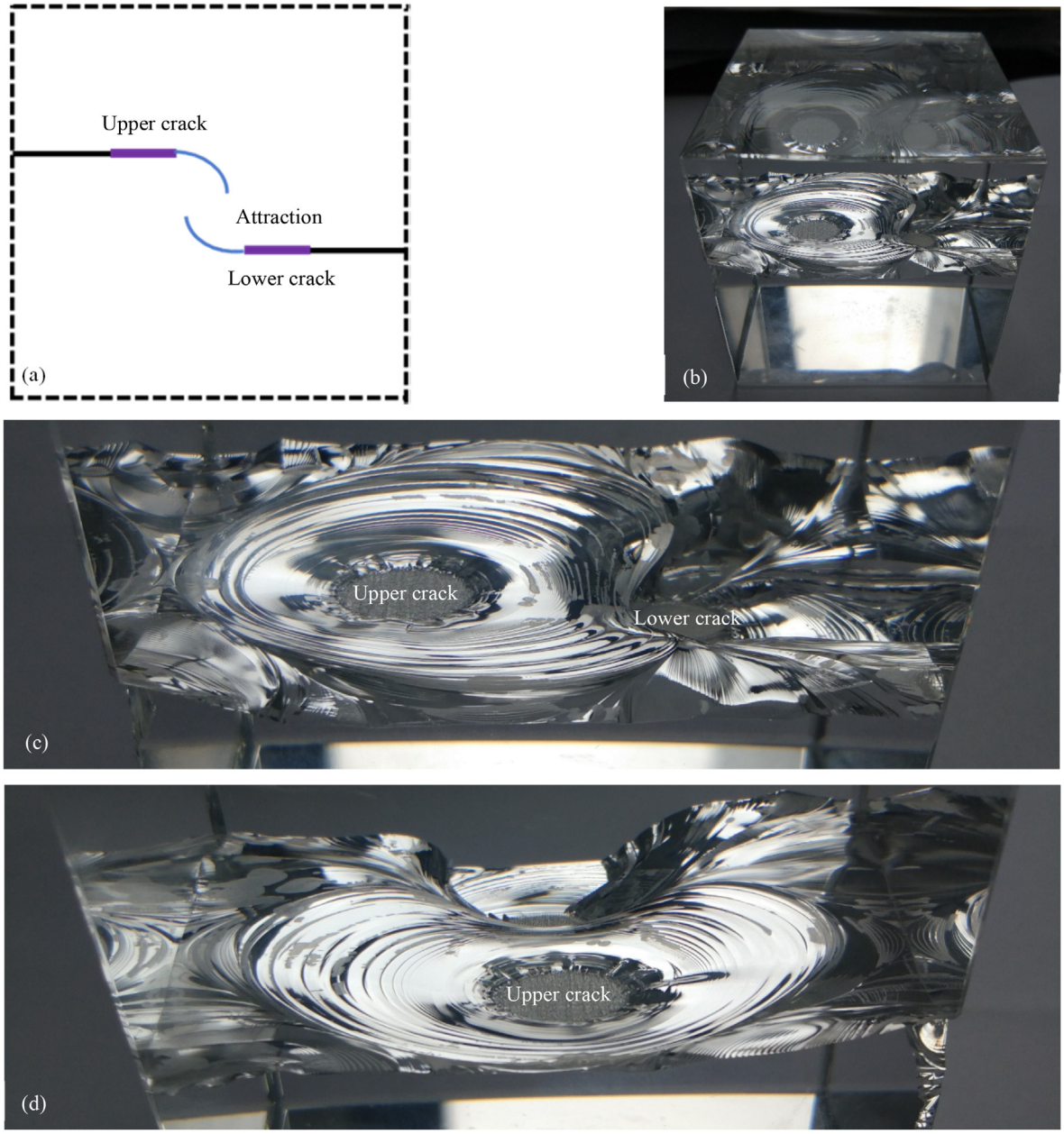

Fig. 6. Attraction of two internal cracks under ultrasonic action: (a) Side view, (b) Oblique view, (c) Local view 1, and (d) Local view 2.

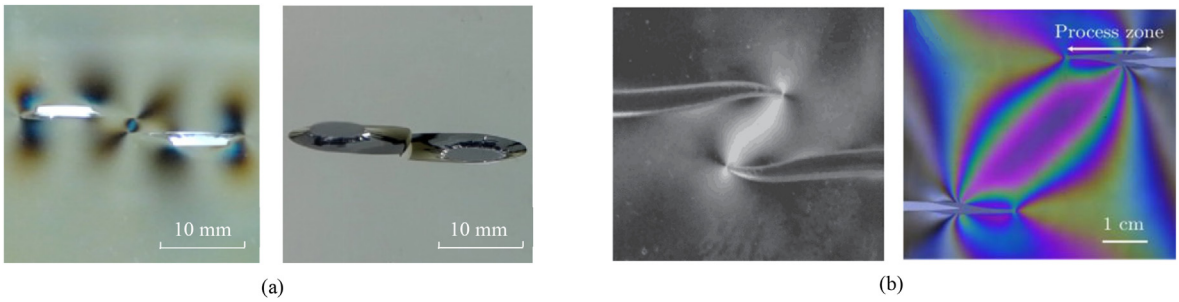

Fig. 7. (a) Attraction of 3D cracks under tension (Yu et al., 2019), and (b) Attraction of 2D cracks under tension (Fender et al., 2010; Dalbe et al., 2015).

3.2. Macro- and micro-fracture characteristics

Viewing the crack fracture as a whole, the fracture can be divided into a crack propagation zone and a transient fracture zone. In the crack propagation zone located around the periphery of the prefabricated crack, the beach marks are often closed-loop, the shape is clear and uniform, the surface is relatively flat, and the fluctuation is small. A transient fault zone was observed outside the

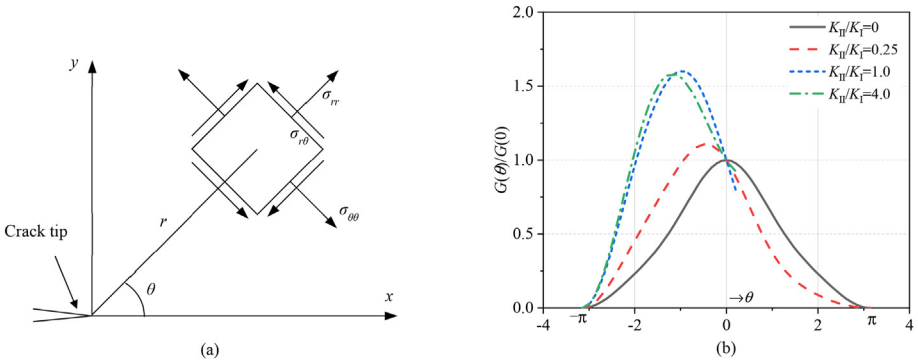

Fig. 8. Crack deflection under mixed mode I-II loading: (a) Stress field around the crack tip, and (b) Normalized mechanical energy release rate varying with deflection angle. $G(0)$ is the mechanical energy release rate at angle $\theta = 0$.

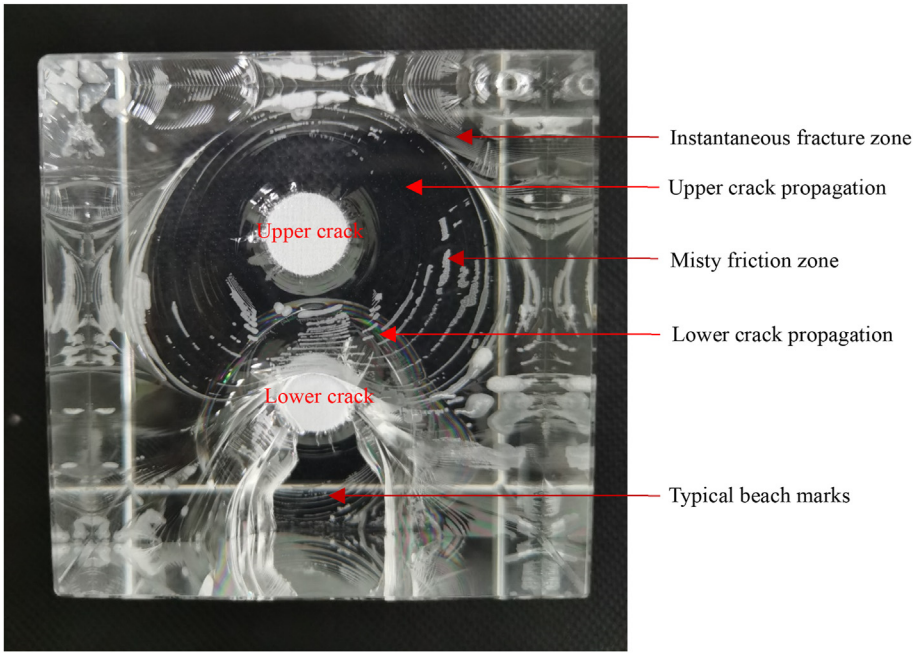

Fig. 9. Top view of samples after UF action.

crack propagation zone, and it is located at the edge of the sample. The beach marks are line segments connected to the sample surface, indicating that they do not form a closed loop, their shape is not uniform, and the surface is undulating.

Both the instantaneous fault zone and crack propagation zone exhibit the following characteristics: (i) fatigue beach marks, (ii) mode III fractures, and (iii) fog-like friction zone. The three characteristics are described in detail below, and their formation mechanisms were investigated.

3.2.1. Fatigue beach marks

The normal direction of fatigue beach marks is consistent with the crack propagation direction and crack propagation path, i.e. each beach mark corresponds to the expansion of a crack caused by the application of a reciprocating load, and the beach marks are fatigue fractured. Typical fracture characteristics are present. Meanwhile, considering the frequency of the ultrasound in this study, the ultrasonic loading can be regarded as a high-frequency and high-cycle fatigue loading (Liu and Dai, 2021). The beach marks of glass in Fig. 10 are more likely the pattern of mixed mode I-II brittle fracture rather than the plastic deformation trace resulting from the local plastic yield at the crack tip due to the changes in the state and magnitude of stress, and are rather common on the metal fracture surface. Similar features called rib marks were observed on the rock fracture surface (Shang et al., 2017). When high-frequency elastic waves are generated into a specimen by ultrasonic waves, the elastic waves can be divided into two types: longitudinal waves perpendicular to the internal crack surfaces and transverse waves parallel to the internal crack surfaces. The longitudinal waves open and close the cracks repeatedly in a small amplitude, inducing crack growth in a plane. Transverse waves that are perpendicular to the crack growth plane disturb the crack growth path, ultimately resulting in fatigue fracture with undulating beach marks.

Along the crack propagation direction, the beach marks become more and more sparse, with gradual increase in spacing. It can be concluded that under the same ultrasonic load, as the crack grows, the larger the size of the crack, the larger the crack expansion step, i.e. the growth rate is directly proportional to the crack size. This also conforms to the basic principle of fatigue fracture mechanics. Overall, the beach marks of the upper crack are denser than those of the lower crack.

The beach marks are denser in the region where the cracks attract each other and the upper cracks expand downward than

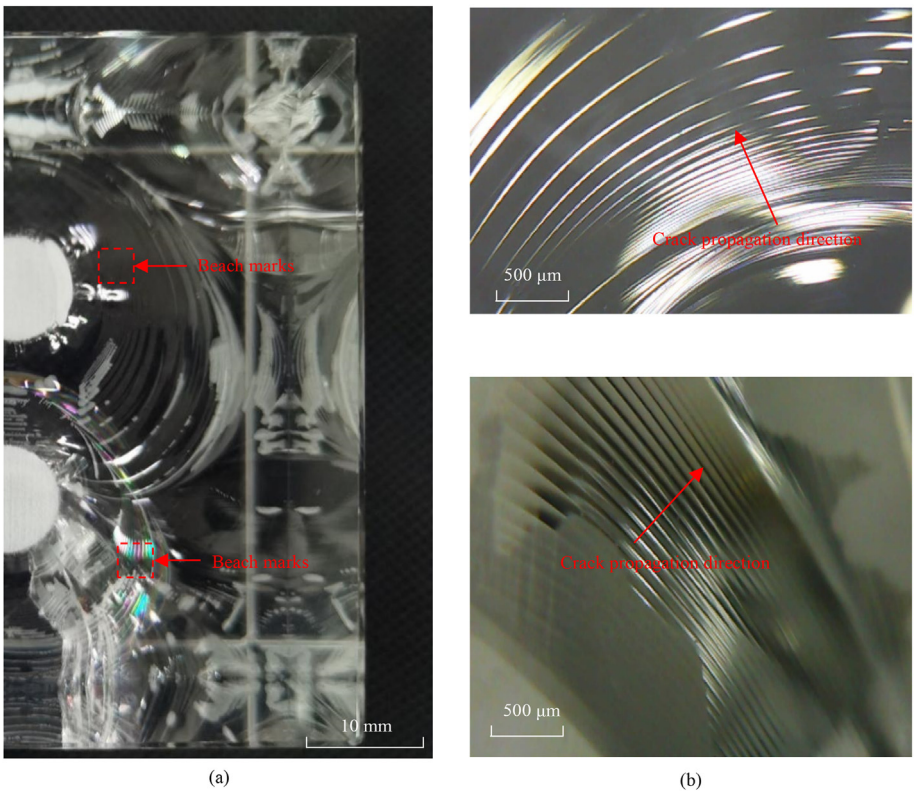

Fig. 10. Fatigue beach marks: (a) Beach marks on the fracture surface, and (b) Partial enlarged drawing.

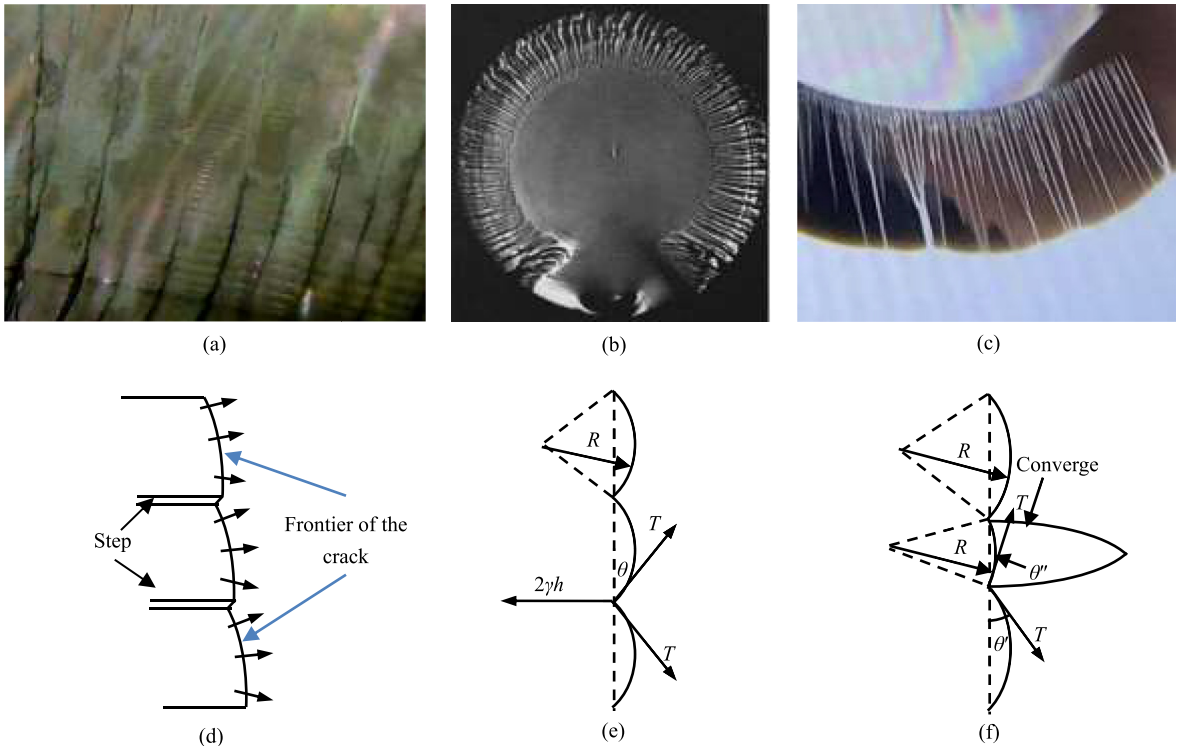

Fig. 11. Mode III fracture characteristics: (a) Lance-like patterns on the fracture surface, (b) Lance-like patterns in Sommer (1969), (c) Lance-like patterns in Wang et al. (2020)a,b, (d) Bending between steps, (e) Balance force on evenly spaced steps, and (f) Converge of lance-like pattern on unevenly spaced steps.

those in other regions. Near the mutual attraction zone, the upper crack beach marks are thinner than those in their area, forming a realistic "heart-shaped" feature. In the expansion area, each beach mark is closed, and the spacing and shape change gently. However, the regularity remains consistent. The beach marks in the instantaneous fault zone are connected to the surface of the sample. It is a

line segment, and the spacing and shape change drastically and irregularly. The center of the beach marks in the instantaneous break zone is in the direction of the edge or corner of the sample and is in the exact opposite direction of the extended zone.

3.2.2. Mode III fracture

As shown in Fig. 11a, "lance-like" patterns were observed between some beach marks. Generally, "lance-like" pattern is the typical characteristic of mode III fracture, as shown in Fig. 11b (Sommer, 1969) and c (Wang et al., 2020a, b). It was speculated that mode III fracture appeared on the crack surface under UF.

Unlike the continuous adjustment of crack surface along the entire crack front under mode II loading, the propagating crack under mixed mode I-III loading tends to rotate on an axis parallel to the direction of the fracture and breaks into partial surfaces, hence forming the so-called "steps" between the discontinuous twisted surfaces, as shown in Fig. 11d. Friedel and Smoluchowski (1957) analyzed the formation of lance-like patterns based on the dislocation theory that could be applied to amorphous solids by considering either the scale or microstructure. During the crack propagation, the elastic strain energy at the crack tip is greater than that in other regions, i.e. additional energy is needed for crack propagation between the steps. In other words, the line tension T at the crack front is the unit energy required for crack propagation per unit length. Fig. 11d–f shows the schematic diagrams for the formation of lance-like patterns. θ is the angle between the front arc of the crack propagation on an evenly distributed step and the initial horizontal plane of crack propagation; θ' and θ'' are the included angle between the front arc of crack propagation on large and small spacing step and the initial horizontal plane of crack propagation, respectively. The shape of the step is shown in Fig. 11d, where the arrow indicates the expansion direction of the bending edge of the step. The drag force of the step is $2\gamma h$, where γ is the energy required to form a unit surface at the step and h is the height of the step. For evenly spaced steps, $\theta'' = \theta' = \theta$. The condition for the propagation of whole crack front can be expressed as follows (Friedel and Smoluchowski, 1957):

$$2\gamma h = 2T \sin\theta \tag{4}$$

As the crack front moves forward, the crack frontier bends constantly, subsequently forming a step. In fact, the lance-like pattern observed on the fracture surface should be the strips connecting the adjacent cracks, i.e. the superposition of the adjacent surfaces. With the propagation of crack, the torsion angle of the newly formed surface enlarges, i.e. a higher altitude of the steps. The fractured surfaces show that the tiny lances converge just like branches merging into the main stream, as shown in Fig. 11f. The confluence direction is consistent with the crack propagation direction.

One interesting phenomenon unlike the mixed mode I-III fracture under static load is that the edges of lance-like patterns in the experiments in this study were observed to be rough with white powder similar to rime or snow on the tree branches in winter (Fig. 12d), proving the violent friction of the fracture surface under the ultrasonic action.

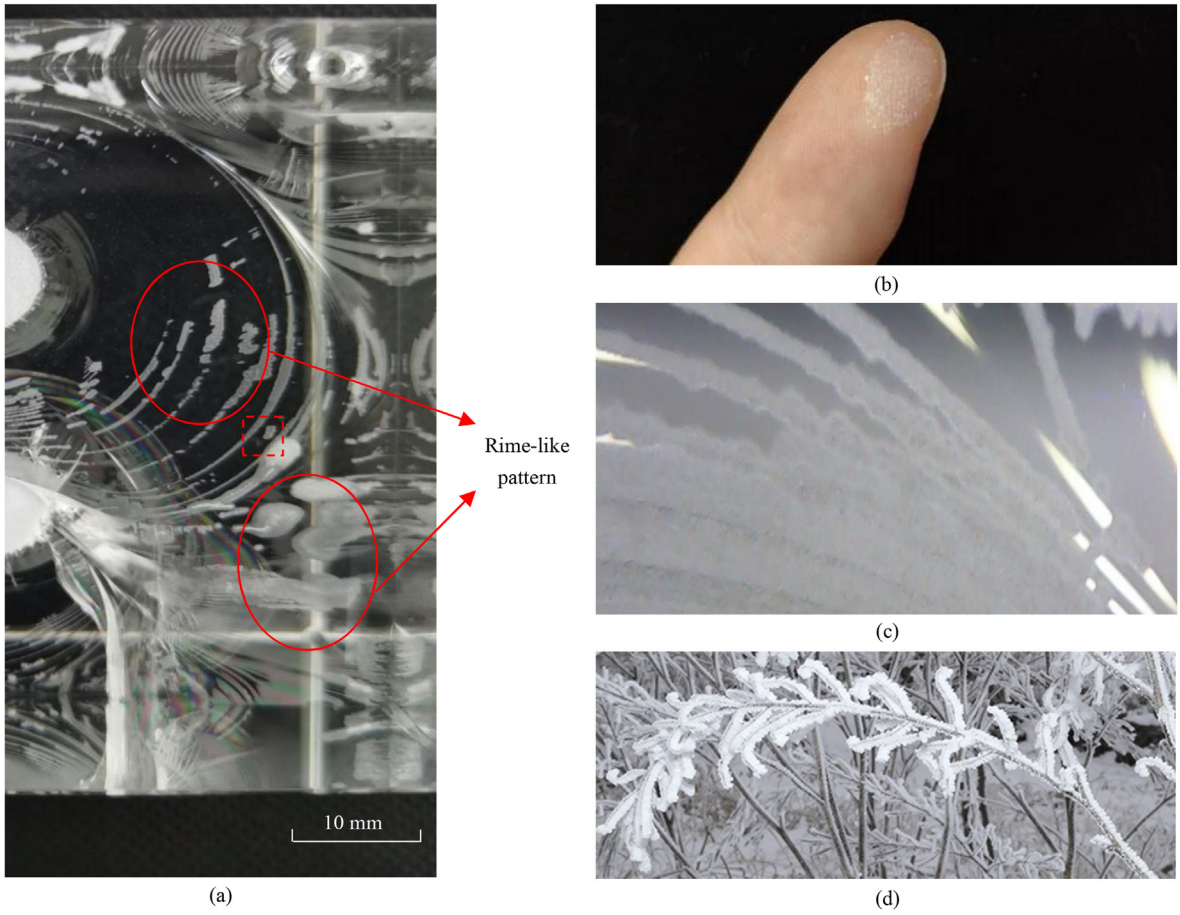

Fig. 12. White spotted foggy area: (a) Local white spots, (b) Powder, (c) Partial enlarged drawing, and (d) Rime.

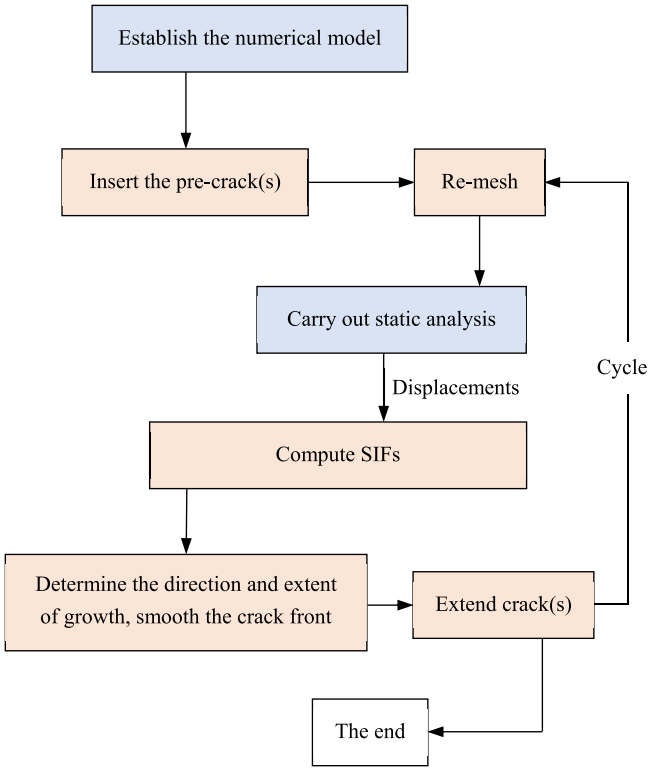

Fig. 13. Flowchart of numerical simulation. The grey-blue box denotes that the step is finished in Abaqus and the light orange box denotes that the step is finished in FRANC3D.

3.2.3. *White spotted foggy area*

Local white spots were observed on the extension surface, mainly comprising scalloped arcs and edges. The characteristics of the white spots on the crack growth under UF were determined. At present, in this study, a single crack growth test under UF was conducted, indicating that under the ultrasonic high-frequency alternating load, crack tip grows, and the crack contact surface undergoes severe friction. In addition, the temperature rise induced by the friction can also be a factor of the deterioration of the material (Zhu et al., 2021).

The white spotted foggy area was gently wiped by hand to remove the powder on the surface (Fig. 12). A white hazy area is formed by friction on the cracked surface.

On the macro-fracture, most white spots are distributed along the beach marks, and some white spots are connected to a region with different lengths and areas.

Microscopically, along the III-mode steps at the local mode III steps, the haze area also often appears.

4. Numerical simulation

As mentioned in Section 1, UF experiments lack intuitive and visual experimental methods, numerical simulation in the UF field is very difficult. The lack of the comparable physical test results leads to the superficiality of simulation goals in numerical modeling. In addition, the internal crack problem is often a 3D problem. Its extended path simulation involves internal crack modeling, fracture criteria, grid disconnection, and many other issues. These challenges coupled with “special” loads such as ultrasound make the issues more complex.

In this study, a discontinuous medium mechanics method was used to establish a numerical simulation method based on the fatigue fracture mechanism. The simulation of double crack propagation path under ultrasonic treatment was conducted and compared with the test results. Abaqus and FRANC3D were used jointly during the numerical simulation, as shown in Fig. 13. To be more specific, the procedure is divided into five steps:

(1) A linear elastic model of the sample with structure grid and boundary conditions was established in Abaqus.
(2) Import the model in FRANC3D, then insert the internal crack, and re-mesh the model with internal cracks.
(3) Call Abaqus to perform calculation to obtain the stress distribution, from which FRANC3D calculates the SIFs on crack tips, kink angle, and extent of crack growth to form a new crack tip.
(4) Repeat Step 2 according to the new crack tip, and repeat the re-mesh step to obtain a model with updated grid.
(5) Repeat Steps 3 and 4, and calculate cyclically to obtain the crack propagation path.

4.1. *Numerical model*

A simulation model was established, and the finite element mesh is shown in Fig. 14. The model size was 60 mm × 60 mm × 60 mm, and the radius of internal cracks is 5 mm, the same as that

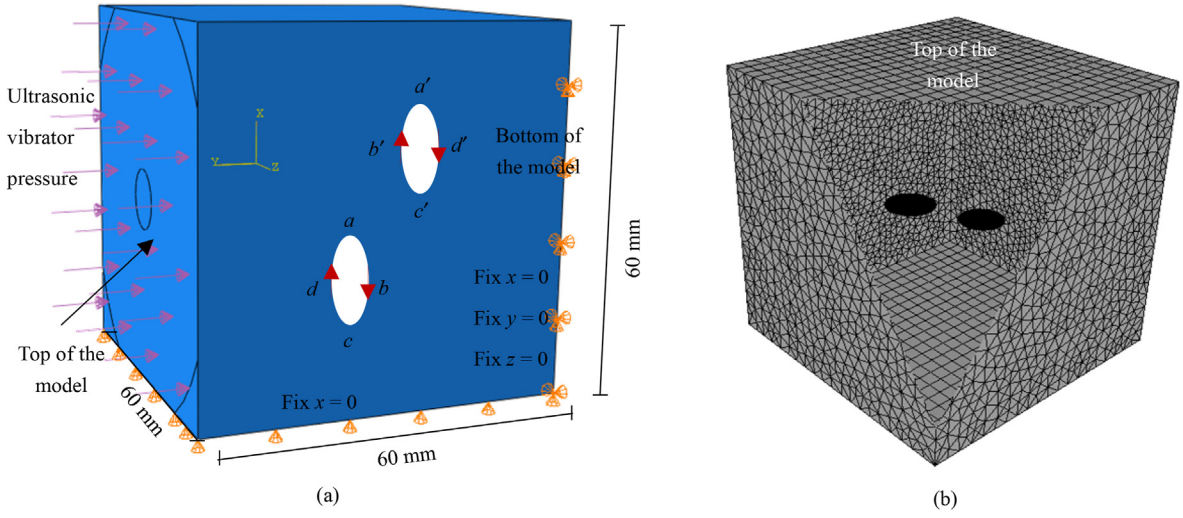

Fig. 14. (a) Boundary condition and (b) grid of the model with internal cracks.

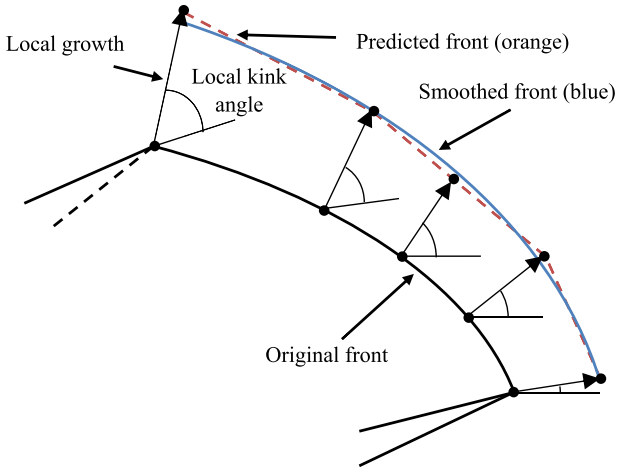

Fig. 15. Process of crack growth and crack tip fitting.

of the real sample. The material property is linear elasticity with an elastic modulus E of 82 GPa and Poisson's ratio ν of 0.21. The bottom of the model (right surface shown in the diagram) and downward surface were fixed to limit the displacement, while the displacement-controlled loading was applied on the top of the sample (left surface shown in the diagram), as shown in Fig. 14a. The boundary conditions are based on the experiment. The bottom of the sample is compressed by the clamp; therefore, the x, y and z directions were constrained. The downward surface acts as the pressure-bearing surface, resisting the tendency of falling due to gravity of the sample; therefore, a constraint was also set in the x direction. Considering the ultrasonic vibration amplitude, a displacement-controlled loading of 0.02 mm was set on the top of the model in Abaqus. Then, in FRANC3D, the fatigue model with crack growth load schedule was established. The SIF ratio in the fatigue model is $R = -1$; therefore, the initial uniaxial compression turns into the alternating compression-tension load. Moreover, the fatigue model in FRANC3D was set as time-independent, thus a persistent repeat of alternating load aiming at simulating the ultrasonic load was specified. According to the experimental scheme, numerical simulations of models with internal cracks of different depths were carried out.

4.2. Fatigue crack propagation model

The Paris model is a fatigue crack propagation model proposed by Paris and Erdogan (1963) and can be expressed as follows:

$$\frac{da}{dN} = C(\Delta K)^n \tag{5}$$

where a is the crack length; N is the circulating cycle of the alternating load; da/dN is the crack propagation rate; C and n are the material fatigue parameters, with the values of 1.5×10^{-10} and 3.8, respectively; and $\Delta K = K_{max} - K_{min}$ represents the SIF amplitude.

4.3. Calculation of SIF

In three dimensions, the J-Integral was evaluated within a cylindrical domain centered on a portion of the crack front. The J-integral can be expressed as follows (Rice, 1968):

$$J = \int_{\Gamma} \left(W dy - T_i \frac{\partial u_i}{\partial x} ds \right) \tag{6}$$

where Γ is the integration path, W is the strain energy density, T_i is the traction vector, u_i is the displacement vector, and ds is the differential arc length along Γ. Considering the conditions of small-scale yielding, the J-integral is equal to the energy release rate. The finite element SIFs can be solved from Eq. (6) based on the calculating methods (Li et al., 1985; Banks-Sills et al., 2007) developed after Rice's work.

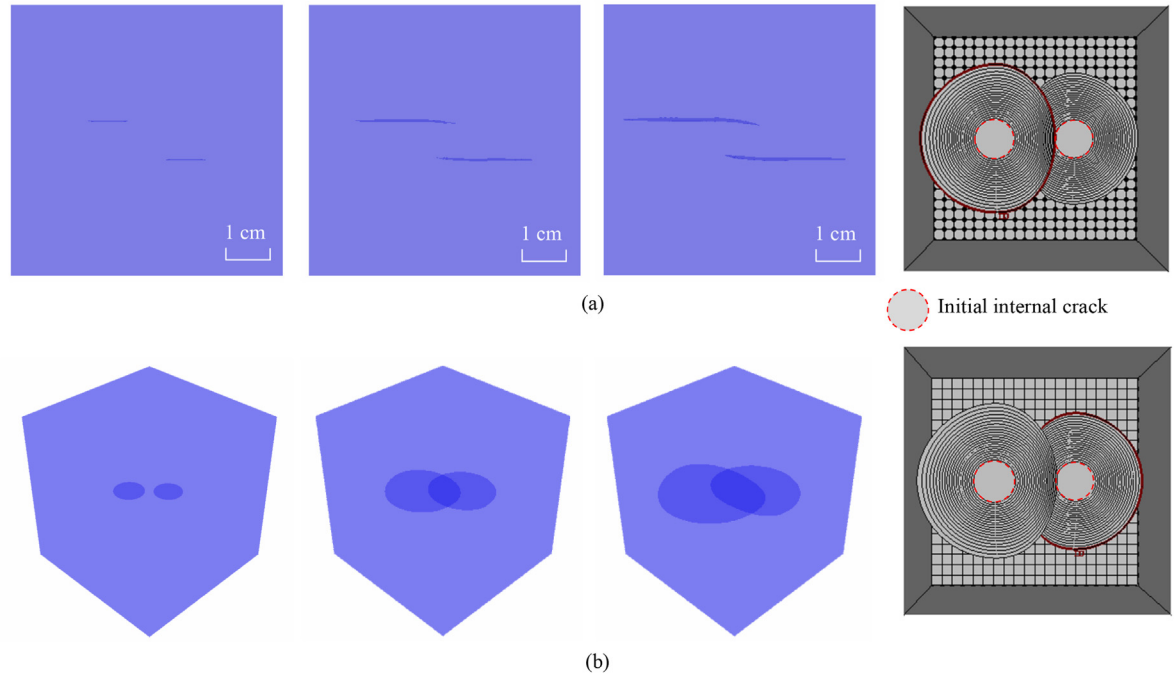

Fig. 16. Simulation of crack path: (a) Front view of the crack surface expansion shape, and (b) Side view of the crack growth.

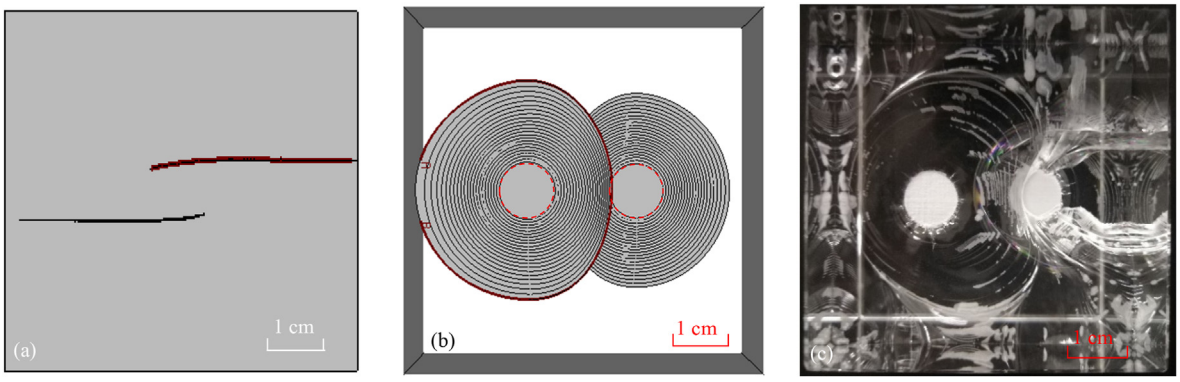

Fig. 17. Comparison between numerical simulation and physical experimental results: (a) Front view of attraction of the cracks, (b) Top view of crack growth path of the cracks in numerical simulation, and (c) The attraction of the cracks observed in the experiment.

4.4. Method for simulating crack propagation path

Fig. 15 shows the schematic diagram of the simulation strategy to determine the crack propagation path. The calculation process can be divided into three steps:

(1) Based on the maximum tensile stress (MTS) criterion shown in Section 4.4.1, the crack kink angle θ is obtained.
(2) The calculation of expansion step size is determined by user based on the calculation method provided in Section 4.4.2.
(3) Once the crack kink angle and expansion step size of each point are obtained, a new crack tip line is predicted, as shown by the orange dashed line in Fig. 15. Then, smoothed processing was performed using polynomial fitting, and the smoothed crack tip is shown as the blue line in the figure.

4.4.1. MTS criterion

The MTS criterion was used to determine the direction of crack growth, and the crack will propagate along the orientation of the maximum hoop stress $\sigma_{\theta\theta\max}$. The maximum hoop stress can be expressed as follows (Lawn, 1993):

$$\sigma_{\theta\theta\max} = \frac{\cos(\theta/2)}{2\sqrt{2\pi r}}[K_{\mathrm{I}}(1+\cos\theta) - 3K_{\mathrm{II}}\sin\theta] \tag{7}$$

where θ is the crack kink angle when $\sigma_{\theta\theta}$ reaches the maximum value. The angle θ can also be obtained directly:

$$\theta = 2\arctan\frac{1-\sqrt{1+8(K_{\mathrm{II}}/K_{\mathrm{I}})^2}}{4(K_{\mathrm{II}}/K_{\mathrm{I}})} \tag{8}$$

4.4.2. Calculation of crack growth size

The crack growth length Δa_i of a certain point i at the crack edge can be determined by the formula as follows (Fracture Analysis Consultants, 2019):

$$\Delta a_i = \Delta a_{\mathrm{median}}\frac{\frac{\mathrm{d}a}{\mathrm{d}N_i}(\Delta K_i, R_i, K_{\max}, \ldots)}{\frac{\mathrm{d}a}{\mathrm{d}N_{\mathrm{median}}}(\Delta K_{\mathrm{m}}, R_{\mathrm{m}}, K_{\max}, \ldots)} \tag{9}$$

where $\Delta a_{\mathrm{median}}$ is a user-specified parameter, which is the median of extension lengths of the calculation point with the default value of 15% length of the radius of the crack; $\mathrm{d}a/\mathrm{d}N_{\mathrm{median}}$ is the crack growth rate computed at the crack front point with the median SIF value; ΔK_i and R_i are the increments of SIFs and stress ratio at point i, respectively; while ΔK_{m} and R_{m} are the medians of SIFs and stress ratio of all the points, respectively; and $K_{\max}$ is the maximum SIFs in the calculation process.

4.5. Simulation results

4.5.1. Expansion path under double crack interaction

The crack growth is shown in Fig. 16. A comparison between the numerical analysis and physical test is shown in Fig. 17. The following observations were made:

(1) The parallel internal crack tips attract and draw each other nearer, showing a “hook shape” in space, and the overall shape is consistent with the physical tests.
(2) With increasing crack propagation area, in the non-interaction zone, the step length of each step under the same load increases in size. Moreover, in the interaction zone, the propagation speed decreases, and this observation is consistent with the physical test results.
(3) The upper crack propagation area is larger than the lower crack propagation area and is consistent with the test results.

4.5.2. Distribution law of SIF

$K_{\mathrm{I}}/|K_{\mathrm{Imax}}|$ was used to study the distribution law of SIF, where $|K_{\mathrm{Imax}}|$ is the maximum value of K_{I} in the calculation. Noting that every single curve in Fig. 18 represents the normalized K_{I}

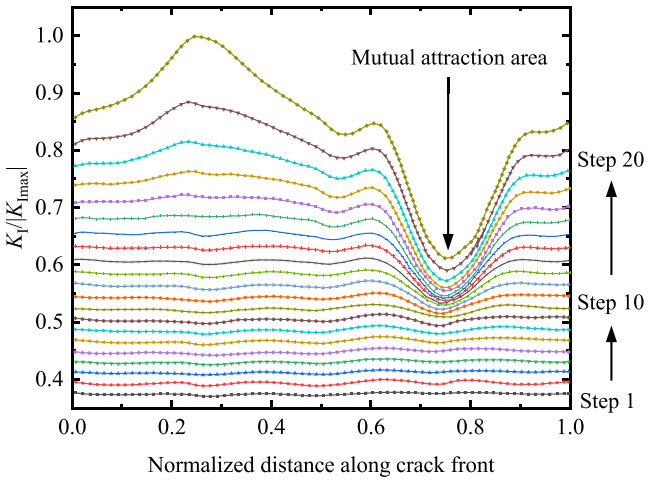

Fig. 18. Normalized SIF distribution.

distribution of each step. The rule is shown in Fig. 18 and can be described as follows:

(1) At each expansion step, the upper crack tip K_I is larger than the lower crack tip K_I. Thus, the upper crack tip begins to crack first, and the propagation surface is larger than the lower crack, consistent with the results of physical tests.
(2) Overall, the K_I becomes larger with increasing crack area from step 1 to step 20, consistent with the sparseness of beach marks in the test.
(3) When the crack propagation area has yet to reach a certain level, K_I basically shows no change along the crack tip, indicating that mutual attraction has not yet occurred. This is consistent with the phenomenon that the bevel line is circular when the loading is initiated in the physical test.
(4) When the crack grows to a certain extent, in the crack tip area on the center side, first the two crack tips K_I rise slightly and then fall. This is consistent with the sparseness of beach marks and the denseness of beach marks in the mutual attraction area in the physical tests.
(5) In the non-active area, when the distance is farther away from the active area, the value of K_I is larger and is consistent with the sparseness of beach marks in the non-active area in the physical tests.

5. Conclusions

The experiments and numerical simulations of the two internal cracks under UF effects revealed the growth path, attraction and the surface characteristics. Some conclusions of this investigation are drawn as follows:

(1) The crack near the ultrasonic excitation source preferentially initiates the cracking, with a faster expansion speed and larger expansion area, forming a failure surface. When the double cracks do not attract, the propagation path is approximately circular, they approach to a certain degree, and mutual “attraction” phenomenon appears forming a “hook shape” in space, while a “heart-shaped” pattern is formed on the plane.
(2) The fracture can be divided into the crack propagation zone and transient fault zone. The beach marks in the crack extension area are closed, while the beach marks in the instantaneous fault area are connected to the surface of the sample as line segments. The center of the beach marks in the instantaneous break zone lies in the direction of the edge or corner of the sample and is in the exactly opposite direction of the extended zone.
(3) The fracture surface is characterized by beach marks, mode III fractures, and a fog-shaped friction zone. The normal direction of beach marks is the same as the crack propagation direction, but the width of the crack propagation zone decreases. In the area where the cracks attract each other, the beach marks are denser than those in other areas. In the region where the crack propagation direction changes drastically, a mode III fracture feature is present. The expansion surface is present in a local white spot area, which is foggy and powdery due to friction.
(4) In terms of mechanical mechanism, based on the fracture characteristics, the physical and mechanical mechanisms for determining crack propagation under ultrasonic field must include an ultrahigh cycle or high-cycle fatigue fracture, crack surface shear, crack surface friction, and temperature rise load.
(5) The Paris fatigue model was used for numerical simulation under UF effects. The results showed that the crack propagation path is consistent with the results of the physical tests, and the K_I distribution based on the J-integral is consistent with the test law.

Declaration of competing interest

The authors declare that they have no known competing financial interests or personal relationships that could have appeared to influence the work reported in this paper.

Acknowledgments

This study was supported by the National Natural Science Foundation of China (Grant Nos. 52104125, U1765204 and 51739008).

References

Adams, M., Sines, G., 1978. Crack extension from flaws in a brittle material subjected to compression. Tectonophysics 49 (1), 97–118.
Banks-Sills, L., Wawrzynek, P.A., Carter, B., 2007. Methods for calculating stress intensity factors in anisotropic materials: Part II - arbitrary geometry. Eng. Fract. Mech. 74 (8), 1293–1307.
Chen, Q., Yao, G., Zhu, H., Tan, Y., Xu, F., 2017. Numerical simulation of ultrasonic wave transmission experiments in rocks of shale gas reservoirs. AIP Adv. 7 (1), 015205.
Dalbe, M.J., Koivisto, J., Vanel, L., et al., 2015. Repulsion and attraction between a pair of cracks in a plastic sheet. Phys. Rev. Lett. 114 (20), 205501.
Dyskin, A., Jewell, R., Joer, H., Sahouryeh, E., Ustinov, K.B., 1994. Experiments on 3-D crack growth in uniaxial compression. Int. J. Fract. 65 (4), 77–83.
Fender, M.L., Lechenault, F., Daniels, K., 2010. Universal shapes formed by two interacting cracks. Phys. Rev. Lett. 105 (12), 125505.
Fracture Analysis Consultants, 2019. FRANC3D Reference Manual. Ithaca, New York, USA.
Friedel, J., Smoluchowski, R., 1957. Les dislocations. Phys. Today 10 (7), 36–39.
Fu, J.W., Chen, K., Zhu, W.S., Zhang, X.Z., Li, X.J., 2016. Progressive failure of new modelling material with a single internal crack under biaxial compression and the 3-D numerical simulation. Eng. Fract. Mech. 165, 140–152.
Gao, M., Xie, J., Gao, Y., et al., 2021a. Mechanical behavior of coal under different mining rates: a case study from laboratory experiments to field testing. Int. J. Min. Sci. Technol. 31 (5), 825–841.
Gao, M., Xie, J., Guo, J., Lu, Y., He, Z., Li, C., 2021b. Fractal evolution and connectivity characteristics of mining-induced crack networks in coal masses at different depths. Geomech. Geophys. Geo-Energy Geo-Resour. 7 (1), 9.
Germanovich, L., Salganik, R., Dyskin, A., Lee, K., 1994. Mechanisms of brittle fracture of rock with pre-existing cracks in compression. Pure Appl. Geophys. 143 (1–3), 117–149.
Griffith, A.A., Taylor, G.I., 1921. The phenomena of rupture and flow in solids. Philos. Trans. R. Soc. A-Math. Phys. Eng. Sci. 221 (582–593), 163–198.
Han, L., Wang, L., Zhang, W., Geng, B., Li, S., 2021. Rockhead profile simulation using an improved generation method of conditional random field. J. Rock Mech. Geotech. Eng. https://doi.org/10.1016/j.jrmge.2021.09.007.
Huang, J.G., Wang, H.G., Ji, G.D., Zhao, F., Ming, R.Q., Hao, Y.L., 2018. The rock breaking mechanism of ultrasonic high frequency rotary-percussive drilling technology. Pet. Drill. Tech. 46 (4), 23–29 (in Chinese).
Ju, Y., Xie, H.P., Zheng, Z.M., et al., 2014. Visualization of the complex structure and stress field inside rock by means of 3D printing technology. Chin. Sci. Bull. 59 (36), 5354–5365.
Lawn, B., 1993. Fracture of Brittle Solids, 2rd ed. Cambridge University Press, Cambridge, UK.
Li, F.Z., Shih, C.F., Needleman, A., 1985. A comparison of methods for calculating energy release rates. Eng. Fract. Mech. 21 (2), 405–421.
Li, G., Hu, Y., Tian, S.M., Ma, W.B., Huang, H.L., 2021e. Analysis of deformation control mechanism of prestressed anchor on jointed soft rock in large cross-section tunnel. Bull. Eng. Geol. Environ. 80, 9089–9103.
Li, H.Z., Wang, H.J., Tang, L., Ren, X.H., Cai, Y.B., 2021d. Fracture of brittle solid material containing a single internal crack of different depths under three-point bending based on 3D-ILC. Eng. Fract. Mech. 248, 107673.
Li, M., Guo, P., Stolle, D., Sun, S., Liang, L., 2021c. Modeling hydraulic fracture propagation in a saturated porous rock media based on EPHF method. J. Nat. Gas Sci. Eng. 89, 103887.
Li, X., Peng, K., Peng, J., Hou, D., 2021a. Experimental investigation of cyclic wetting-drying effect on mechanical behavior of a medium-grained sandstone. Eng. Geol. 293, 106335.
Li, X., Peng, K., Peng, J., Xu, H., 2021b. Effect of cyclic wetting–drying treatment on strength and failure behavior of two quartz-rich sandstones under direct shear. Rock Mech. Rock Eng. 54 (11), 5953–5960.

Lin, Q., Cao, P., Cao, R., Lin, H., Meng, J., 2020a. Mechanical behavior around double circular openings in a jointed rock mass under uniaxial compression. Arch. Civ. Mech. Eng. 20 (1), 19.
Lin, Q., Cao, P., Meng, J., Cao, R., Zhao, Z., 2020b. Strength and failure characteristics of jointed rock mass with double circular holes under uniaxial compression: insights from discrete element method modelling. Theor. Appl. Fract. Mech. 109, 102692.
Lin, Q., Cao, P., Wen, G., Meng, J., Cao, R., Zhao, Z., 2021. Crack coalescence in rock-like specimens with two dissimilar layers and pre-existing double parallel joints under uniaxial compression. Int. J. Rock Mech. Min. Sci. 139, 104621.
Liu, Y., Dai, F., 2021. A review of experimental and theoretical research on the deformation and failure behavior of rocks subjected to cyclic loading. J. Rock Mech. Geotech. Eng. 13 (5), 1203–1230.
Nezhad, M.M., Fisher, Q.J., Gironacci, E., Rezania, M., 2018. Experimental study and numerical modeling of fracture propagation in shale rocks during Brazilian disk test. Rock Mech. Rock Eng. 51 (6), 1755–1775.
Paris, P.C., Erdogan, F., 1963. A critical analysis of crack propagation laws. Basic Eng 85 (4), 528–534.
Rice, J.R., 1968. A path independent integral and the approximate analysis of strain concentration by notches and cracks. J. Appl. Mech. 35 (2), 379–386.
Schwaab, M.E., Biben, T., Santucci, S., Gravouil, A., Vanel, L., 2018. Interacting cracks obey a multiscale attractive to repulsive transition. Phys. Rev. Lett. 120 (25), 255501.
Shang, J., Hencher, S.R., West, L.J., Handley, K., 2017. Forensic excavation of rock masses: a technique to investigate discontinuity persistence. Rock Mech. Rock Eng. 50 (11), 2911–2928.
Shi, G., Yang, X., Yu, H., Zhu, C., 2019. Acoustic emission characteristics of creep fracture evolution in double-fracture fine sandstone under uniaxial compression. Eng. Fract. Mech. 210, 13–28.
Sommer, E., 1969. Formation of fracture 'lances' in glass. Eng. Fract. Mech. 1 (3), 539–546.
Tang, Q., Zhao, D., Zhou, Y., Zhang, Z., 2020. Discrete element simulation for investigating fragmentation mechanism of hard rock under ultrasonic vibration loading. Energy Sci. Eng. 8 (11), 3805–3822.
Tang, Z.Q., Zhai, C., Zou, Q.L., Qin, L., 2016. Changes to coal pores and fracture development by ultrasonic wave excitation using nuclear magnetic resonance. Fuel 186, 571–578.
Wang, H.J., Zhang, J., Ren, R., Tang, L., Zhong, L., 2019. Embedded cracks in brittle solids induced by laser-medium interaction (3D-ILC). Chin. J. Geotech. Eng. 41 (12), 2345–2352 (in Chinese).
Wang, H.J., Qi, H., Ren, R., Tang, L., 2021. Stress field of structures withInternal cracks by 3D-ILC technology: experimental and numerical analysis. KSCE Journal of CivilEngineering 2021 (21), 1–12, 0191.
Wang, H.J., Yu, S., Tang, Z., Tang, L., Ren, R., Xu, J., 2020a. Investigation of mode I-II-III fracture of brittle spheres with a 60° internal crack using 3D-ILC. Rock Soil Mech. 41 (5), 1573–1582 (in Chinese).
Wang, S., Zhou, J., Zhang, L., Han, Z., 2020b. Numerical investigation of injection-induced fracture propagation in brittle rocks with two injection wells by a modified fluid-mechanical coupling model. Energies 13 (18), 4718.
Xiao, X.C., Pan, Y.S., Lu, X.F., Yang, X.L., 2013. Mechanism of methane permeability enhance through ultrasonic irradiating on low permeable coal seam. Chinese J. Geophys.-Chin. Ed. 56 (5), 1726–1733.
Yang, W.M., Geng, Y., Zhou, Z.Q., et al., 2020. DEM numerical simulation study on fracture propagation of synchronous fracturing in a double fracture rock mass. Geomech. Geophys. Geo-Energy Geo-Resour. 6 (2), 39.
Yu, S.Y., Wang, H.J., Ren, R., et al., 2019. Propagation of double internal cracks under uniaxial tension based on 3D-ILC. Chin. J. Geotech. Eng. 41 (12), 2367–2373.
Zhao, D.J., Yuan, P., 2018. Research on the influence rule of ultrasonic vibration time on granite damage. J. Min. Sci. 54 (5), 751–762.
Zhou, J., Zhang, L., Pan, Z., Han, Z., 2016. Numerical investigation of fluid-driven near-borehole fracture propagation in laminated reservoir rock using PFC2D. J. Nat. Gas Sci. Eng. 36, 719–733.
Zhou, T., Zhu, J.B., Ju, Y., Xie, H.P., 2019. Volumetric fracturing behavior of 3D printed artificial rocks containing single and double 3D internal flaws under static uniaxial compression. Eng. Fract. Mech. 205, 190–204.
Zhu, C., Lin, Y., Feng, G., 2021. Influence of temperature on quantification of mesocracks: implications for physical properties of fine-grained granite. Lithosphere 2021 (Special 4), 7824057.

Prof. Lei Tang received his PhD degree at China University of Mining and Technology in 1998 and took the position of engineer at Nanjing Hydraulic Research Institute (NHRI) at the same year. He was promoted to senior engineer in 2002, and professor level senior engineer in 2007. In 2008, he worked at Delft University of Technology as a Visiting Scholar. He has worked as a Vice Director of Materials and Structural Engineering Department in NHRI since 2007 and became Director at 2020. He is an editorial board member of *Journal of Hydro-Science and Engineering* and the registered consulting expert of Jiangsu Province, China. He was elected in "333 High-level Talents Training Project" of Jiangsu Province. His research currently focuses on hydraulic structural health diagnosis, mainly including detecting technology and equipment for concrete microcracks, telemetry and equipment for concrete microcracks, detecting and visualizing reinforcement technology and equipment for deep-buried diseases in high dams, and objective index of surrounding rock instability. He had undertaken 5 projects from National Natural Science Foundation of China including the major instrument and equipment project, the major project and the general projects. He has published more than 60 academic papers and 3 books, and obtained 15 national invention patents in recent ten years.